



Cite this: *Nanoscale*, 2022, **14**, 6888

## Template synthesis of dual-functional porous $\text{MoS}_2$ nanoparticles with photothermal conversion and catalytic properties†

Xuefeng Pan,<sup>a,b</sup> Radwan M. Sarhan,<sup>a</sup> Zdravko Kochovski,<sup>a</sup> Guosong Chen,<sup>ID c</sup> Andreas Taubert,<sup>ID b</sup> Shilin Mei<sup>\*a</sup> and Yan Lu<sup>ID \*a,b</sup>

Advanced catalysis triggered by photothermal conversion effects has aroused increasing interest due to its huge potential in environmental purification. In this work, we developed a novel approach to the fast degradation of 4-nitrophenol (4-Nip) using porous  $\text{MoS}_2$  nanoparticles as catalysts, which integrate the intrinsic catalytic property of  $\text{MoS}_2$  with its photothermal conversion capability. Using assembled polystyrene-*b*-poly(2-vinylpyridine) block copolymers as soft templates, various  $\text{MoS}_2$  particles were prepared, which exhibited tailored morphologies (e.g., pomegranate-like, hollow, and open porous structures). The photothermal conversion performance of these featured particles was compared under near-infrared (NIR) light irradiation. Intriguingly, when these porous  $\text{MoS}_2$  particles were further employed as catalysts for the reduction of 4-Nip, the reaction rate constant was increased by a factor of 1.5 under NIR illumination. We attribute this catalytic enhancement to the open porous architecture and light-to-heat conversion performance of the  $\text{MoS}_2$  particles. This contribution offers new opportunities for efficient photothermal-assisted catalysis.

Received 22nd February 2022,  
Accepted 29th March 2022

DOI: 10.1039/d2nr01040b

rsc.li/nanoscale

## Introduction

Over the past decades, solar-driven photothermal conversion has attracted intensive attention, which enables broad applications such as environmental remediation, water desalination and photothermal-assisted catalysis under mild conditions with high efficiency.<sup>1–4</sup> Therefore, it is essential to develop photothermal conversion catalysts that can strongly harvest solar energy ranging from UV to the visible light, and even to the near-infrared light (NIR) to accelerate the degradation of water contaminants by the converted heat.<sup>5–7</sup> In principle, the rational design of efficient photothermal conversion-assisted catalysts includes, but is not limited to, active composition as well as structural optimization. Nowadays, various solar absorbers including plasmonic noble metals (e.g., gold and silver),<sup>8,9</sup> narrow bandgap semiconductors (e.g., copper sulfide and tungsten oxide),<sup>10–12</sup> carbon-based nanostructures (e.g., carbon nanotubes and graphenes),<sup>13,14</sup> and organic com-

pounds (e.g., polyaniline (PANI), polypyrrole and polydopamine (PDA)) with outstanding photothermal conversion performance are successfully fabricated.<sup>15–17</sup> For instance, a bismuth vanadate photocatalyst modified with PANI was applied in the water oxidation reaction under NIR light irradiation. The water oxidation photocurrent was increased by more than 300% than that of pristine catalysts with the assistance of photothermal heating of PANI.<sup>17</sup> Recently, our group has successfully developed a gold@PDA nanoreactor for the fast reduction of 4-nitrophenol (4-Nip). The photoheating caused by PDA under NIR irradiation greatly enhanced the reduction reaction catalyzed by the gold nanoparticles embedded inside the nanoreactor.<sup>18</sup> Generally, the catalyst and the photothermal converter are often two different species according to the above-mentioned reports. A hybridization process is usually required to combine the unique function of each material, which often involves complicated synthetic routes and is undesirable from the economic point of view. Furthermore, the activity of the catalytic species is possibly being impaired due to the modification by the photothermal conversion components, which may reduce the active surface or induce diffusion-controlled sluggish kinetics. Therefore, developing a dual-functional catalyst utilizing its intrinsic photothermal conversion and catalytic properties is in great demand.

Among various photothermal conversion materials, molybdenum disulfide ( $\text{MoS}_2$ ) has shown great potential in the fields

<sup>a</sup>Department for Electrochemical Energy Storage, Helmholtz-Zentrum Berlin für Materialien und Energie, Hahn-Meitner-Platz 1, Berlin 14109, Germany.

E-mail: yan.lu@helmholtz-berlin.de, shilin.mei@helmholtz-berlin.de

<sup>b</sup>Institute of Chemistry, University of Potsdam, Potsdam 14476, Germany

<sup>c</sup>The State Key Laboratory of Molecular Engineering of Polymers and Department of Macromolecular Science, Fudan University, Shanghai 200433, China

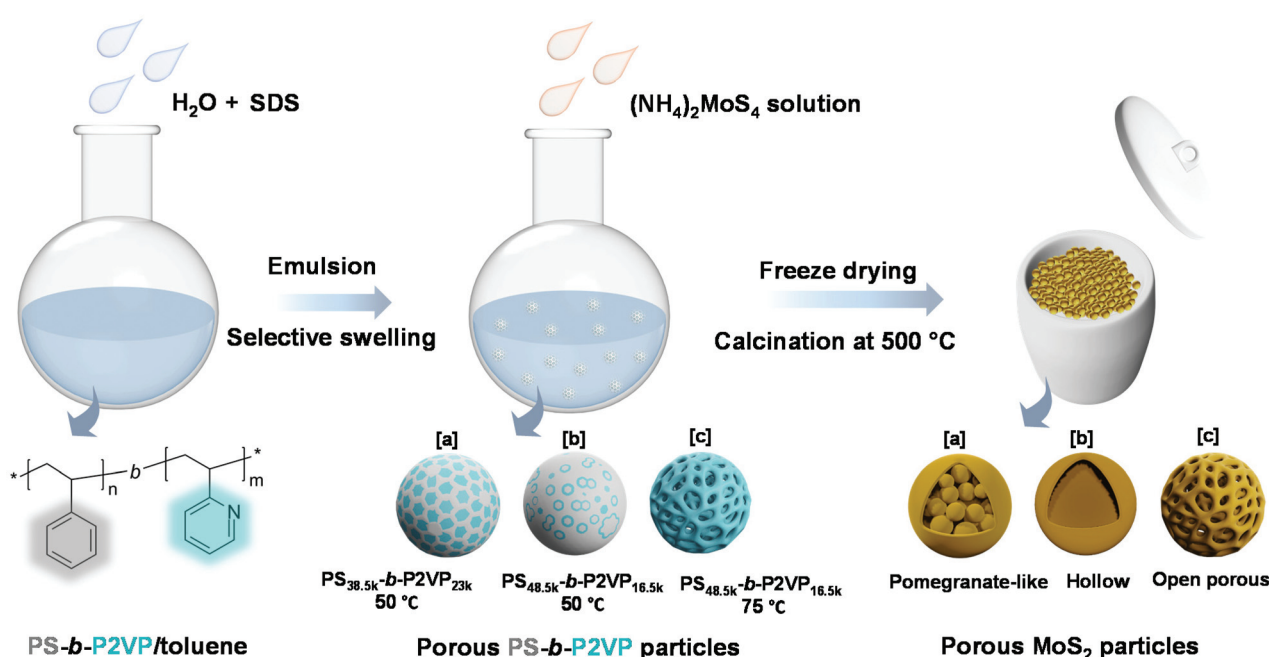
† Electronic supplementary information (ESI) available. See DOI: <https://doi.org/10.1039/d2nr01040b>



of hydrogen generation, pollutant degradation and photothermal therapy due to its tunable chemical and physical properties.<sup>19–24</sup> The photothermal effect of MoS<sub>2</sub> is mainly explained by the generation of electron-hole pairs upon light excitation and their relaxation *via* a non-radiative decay mechanism.<sup>25–27</sup> In addition, MoS<sub>2</sub> exhibits a good catalytic performance in the reduction of 4-Nip.<sup>28</sup> The surface area and crystallinity of the catalytic surface are additional important parameters that determine their performances. Large surface area with a plenty of exposed edges can provide abundant active sites for the catalytic reaction.<sup>29</sup> In addition, metallic 1T-phase MoS<sub>2</sub> has been reported to exhibit a stronger NIR absorption and a higher photothermal conversion efficiency than those of the 2H-phase.<sup>22</sup> However, their instability and tedious synthesis protocol are inevitable. For the more stable 2H phase of MoS<sub>2</sub>, the unsaturated sulfur (S) atoms at the edge sides of MoS<sub>2</sub> nanosheets determine the catalytic activity, while the other S atoms in bulk MoS<sub>2</sub> contribute little to the overall activity.<sup>30,31</sup> Thus, fabrication of MoS<sub>2</sub> with abundant exposed active edges is an effective method to improve the catalytic performance. Furthermore, several approaches including bandgap engineering, defect design, and structural heterojunction *via* hybridization with other nanomaterials such as titanium oxide and nickel oxide have been developed to simultaneously optimize their catalytic and photothermal conversion performance.<sup>26,32,33</sup> Inevitably, these modification approaches also involve complicated synthetic procedures, which lead to additional production costs. Thus, facile fabrication of MoS<sub>2</sub> catalysts with efficient photothermal conversion effects and rich active sites on the catalytic surface remains a challenge.

Recently, it has been revealed that the rational design of nanostructured MoS<sub>2</sub> (*e.g.*, hollow structure) could enable enhanced light scattering and capturing, reduced distance for charge migration, and abundant surface reactive area.<sup>34–36</sup> However, less efforts have been made to explore the more complicated surface/internal nanostructure of MoS<sub>2</sub> due to the limitation of commonly used synthetic methods (*e.g.*, hard template, hydrothermal method, and physical deposition). In contrast, soft templates such as surfactant micelles, organic molecules, and polymer assemblies are good alternatives to prepare novel nanostructures.<sup>37,38</sup> Unlike the harsh conditions needed to remove the hard templates, soft polymer templates can be readily eliminated by solvent dissolution or direct calcination. In particular, block copolymers open up new possibilities for the construction of advanced architectures due to their tunable microphase-separation when serving as soft templates.

In this work, we developed a series of dual-functional MoS<sub>2</sub> particles with well-designed nanostructures, combining the photothermal conversion effect and catalytic property using a soft-template strategy (Scheme 1). Polystyrene-*b*-poly(2-vinylpyridine) (PS-*b*-P2VP) nanoparticles with tunable swollen structures were first fabricated and then used as soft templates.<sup>39</sup> Different volume fractions (determined by the molecular weight) of the P2VP moiety and swelling conditions were applied to tailor the microphase separation of the PS-*b*-P2VP particles, inducing a series of soft templates with significantly different nanostructures.<sup>40</sup> The template can be directly complexed with the ammonium tetrathiomolybdate ((NH<sub>4</sub>)<sub>2</sub>MoS<sub>4</sub>) as the MoS<sub>2</sub> precursor. After calcination, MoS<sub>2</sub> nanoparticles with pomegranate-like, hollow, and open porous structures



**Scheme 1** Synthesis strategy of MoS<sub>2</sub> particles with various morphologies using PS-*b*-P2VP as a sacrificial soft template.

were successfully constructed. The dependence of the photothermal conversion effect as well as the catalytic performance on their morphologies was systematically investigated, demonstrating the importance of structure–property relationship in the photothermal conversion-assisted catalysis.

## Results and discussion

### Material synthesis and characterization

Block copolymers composed of two (or more) covalently bonded homopolymer chains show rich functional groups and microphase separation structure, promoting their increasing application in the formation of ordered hybrid structures and porous functional materials.<sup>41–47</sup> A simple pore-generating method termed “selective swelling” has shown its great potential in extending the micropattern diagram as well as the porous structure of block copolymers.<sup>48,49</sup> The methodology is based on the difference in polarity (or interaction) of the constituent blocks and the swelling solvent. The pores/voids are typically derived from deformed domains of the minor component dispersed in the continuous phase of the major component. In this contribution, PS-*b*-P2VP particles with two different molecular weight fractions of the P2VP moiety were generated by a delicate emulsion-swelling method (Fig. S1a and S1b†). Ethanol, which has strong interaction with the P2VP block but poor interaction with the PS block, was applied as the selective swelling solvent. For PS<sub>38.5k</sub>-*b*-P2VP<sub>23k</sub> and PS<sub>48.5k</sub>-*b*-P2VP<sub>16.5k</sub>, the template particles tend to form solid nanostructures upon swelling in ethanol at 50 °C (Fig. S1c and S1d†). It is also found that dense and spherical P2VP nanodomains (~20 nm) were uniformly distributed inside the polymer particles in PS<sub>38.5k</sub>-*b*-P2VP<sub>23k</sub>. For PS<sub>48.5k</sub>-*b*-P2VP<sub>16.5k</sub>, an irregular hollow space was also generated inside. In this scenario, swelling of both polymer particles results in only slight deformation, and therefore, no porous structures were obtained under this mild condition (Fig. 1a and b). This is mainly due to the slight swelling degree of the P2VP chains at this temperature (50 °C). Moreover, the osmotic pressure of the slightly swollen P2VP domains is too weak to drive the plastic deformation of the rigid PS domains. Therefore, solid or non-porous complex nanostructures of MoS<sub>2</sub> can be expected using these featured polymer particles as templates for the subsequent step of MoS<sub>2</sub> generation. Notably, when the temperature increased from 50 to 75 °C, an open porous nanostructure with interconnected micellar fibers was fabricated (Fig. 1c). At this temperature, a strong chain movement is triggered, which gives rise to the structural reorganization of the polymer chains into network-like spheres. Accordingly, an open porous structure of MoS<sub>2</sub> particles can be obtained by applying these porous particles as synthetic templates. Note that a lower temperature (30 °C) led to a slight swelling of the polymer chains, which is similar to that performed at 50 °C (Fig. S1e†). In contrast, a higher temperature (90 °C) led to the deformation of the polymer particles (Fig. S1f†).

Block copolymers have been reported to serve as templates for the synthesis of nanoparticles *via* coordination with inorganic precursors.<sup>50,51</sup> Benefiting from the good affinity of the P2VP block to the inorganic precursors, anionic MoS<sub>4</sub><sup>2-</sup> was simply complexed with the PS-*b*-P2VP template with selective loading onto the P2VP domain.<sup>52,53</sup> After the thorough incorporation of a molybdenum precursor into the PS-*b*-P2VP particle, the introduction of a trace amount of H<sup>+</sup> and 3-MPA into the solution leads to the decomposition of MoS<sub>4</sub><sup>2-</sup> into MoS<sub>x</sub> (x = 2–3). In this experiment, 3-MPA can serve as a stabilizer and prevent the aggregation of the composite particles. Finally, MoS<sub>2</sub> particles with various internal nanostructures were obtained after calcination in an argon atmosphere. During the calcination step, MoS<sub>4</sub><sup>2-</sup> was pyrolyzed into MoS<sub>2</sub> as the backbone, while much of the polymer template was calcined, leaving a small amount of carbon residues and hollow channels. For PS<sub>38.5k</sub>-*b*-P2VP<sub>23k</sub> particles swollen at 50 °C, MoS<sub>4</sub><sup>2-</sup> cations diffused inside the polymer particle and coordinated with small spherical P2VP domains due to the relatively large volume fraction of the P2VP block (37.4%), compared to PS<sub>48.5k</sub>-*b*-P2VP<sub>16.5k</sub> with a fraction of 25.4%. This results in the formation of pomegranate-like nanoparticles (PLNPs) that contain a solid outer layer (~25 nm thick) with numerous dense nanospheres (~30 nm) inside, as shown in Fig. 1d and g. A limited free space was also observed in PLNPs. In contrast, MoS<sub>2</sub> hollow nanoparticles (HNPs) were obtained using PS<sub>48.5k</sub>-*b*-P2VP<sub>16.5k</sub> particles swollen at 50 °C as templates (Fig. 1e). The HNP particles possess a thin layer of MoS<sub>2</sub> shell (~9 nm), without any visible internal MoS<sub>2</sub> spheres (Fig. 1h). The observed small particles also exhibit the same internal structure as the big ones (Fig. S2a† and 2b). This might be ascribed to the fact that few MoS<sub>4</sub><sup>2-</sup> cations can diffuse into the internal part of PS<sub>48.5k</sub>-*b*-P2VP<sub>16.5k</sub> particles primarily limited by their thicker blocking layer (rigid PS layers) compared with PS<sub>38.5k</sub>-*b*-P2VP<sub>23k</sub>. When it comes to PS<sub>48.5k</sub>-*b*-P2VP<sub>16.5k</sub> particles swollen at 75 °C, the MoS<sub>2</sub> porous nanoparticles (PNPs) preserve the original loose structure of the polymer template (Fig. 1f). Due to the free space between interlocked fibers, the MoS<sub>4</sub><sup>2-</sup> cations can easily diffuse and adsorb onto the internal part of the porous polymer template. After calcination, the polymer was burnt out leading to the formation of the MoS<sub>2</sub> particles with multi-interconnected hollow channels (Fig. 1i). The open porous MoS<sub>2</sub> particles with an interconnected hollow channel structure show several advantages when compared with particles of other morphologies including high porosity, light weight, and large accessible surface area. These are of special relevance to the practical applications including drug delivery, water purification, and surface catalysis. To further optimize the particle structure, we successfully tuned the thickness of the deposited MoS<sub>2</sub> layers by varying the concentration of the inorganic precursor during the synthesis. Fig. 2a–c show the SEM images of a series of MoS<sub>2</sub> particles prepared with different MoS<sub>4</sub><sup>2-</sup> concentrations. The MoS<sub>2</sub> PNPs prepared with different concentrations of (NH<sub>4</sub>)<sub>2</sub>MoS<sub>4</sub> (1, 1.5, and 3 mg mL<sup>-1</sup>) are denoted as MoS<sub>2</sub>-1, MoS<sub>2</sub>-1.5 and MoS<sub>2</sub>-3 PNPs, respectively. These three samples



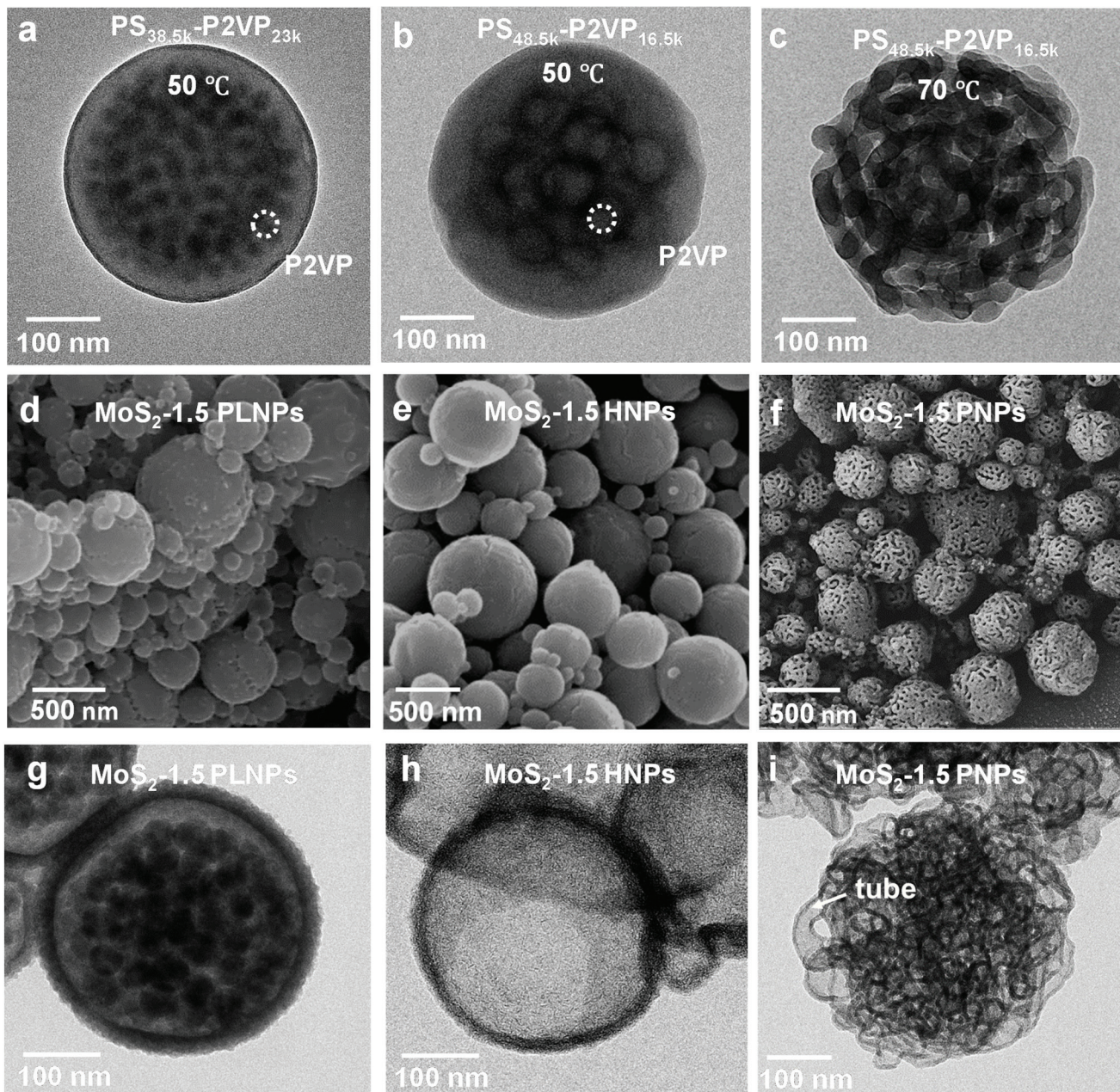


**Fig. 1** TEM images of (a) PS<sub>38.5k</sub>-*b*-P2VP<sub>23k</sub> and (b) PS<sub>48.5k</sub>-*b*-P2VP<sub>16.5k</sub> particles obtained by swelling at 50 °C, and (c) PS<sub>48.5k</sub>-*b*-P2VP<sub>16.5k</sub> particles obtained by swelling at 75 °C. The polymer particles were stained with I<sub>2</sub> vapor for 20 min. The dark contrast shows the distribution of P2VP domains. (d) SEM and (g) TEM images of the MoS<sub>2</sub>-1.5 PLNPs. (e) SEM and (h) TEM images of the MoS<sub>2</sub>-1.5 HNPs. (f) SEM and (i) TEM images of the MoS<sub>2</sub>-1.5 PNPs.

show a broad size distribution with a similar trend that the diameter of the majority concentrates between 200 and 500 nm (Fig. S2c-e†). By increasing the precursor concentration, more MoS<sub>4</sub><sup>2-</sup> were coordinated onto the PS-*b*-P2VP particles and the distance between the separated micellar fibers became narrower. The layer thickness of the hollow channels in the particles increased from ~7 to 12 nm on average, when the concentration of precursor increased from 1 to 3 mg mL<sup>-1</sup>. The presence of tiny MoS<sub>2</sub> flakes with generally single-layered

structures was identified from the HRTEM images (Fig. 2d), suggesting the abundance of exposed active edges. The outer and inner diffraction rings as observed from the selected-area electron diffraction (SAED) pattern correspond to the (110) and (100) reflection of MoS<sub>2</sub>, respectively (Fig. 2e). It is worth noting that the isolated MoS<sub>2</sub> nanoflakes (short sheets of length ~5 nm) of the MoS<sub>2</sub>-1.5 PNPs might be favorable for the utilization of active edges. Carbon generated from the polymer template during calcination also prevents the aggregation of



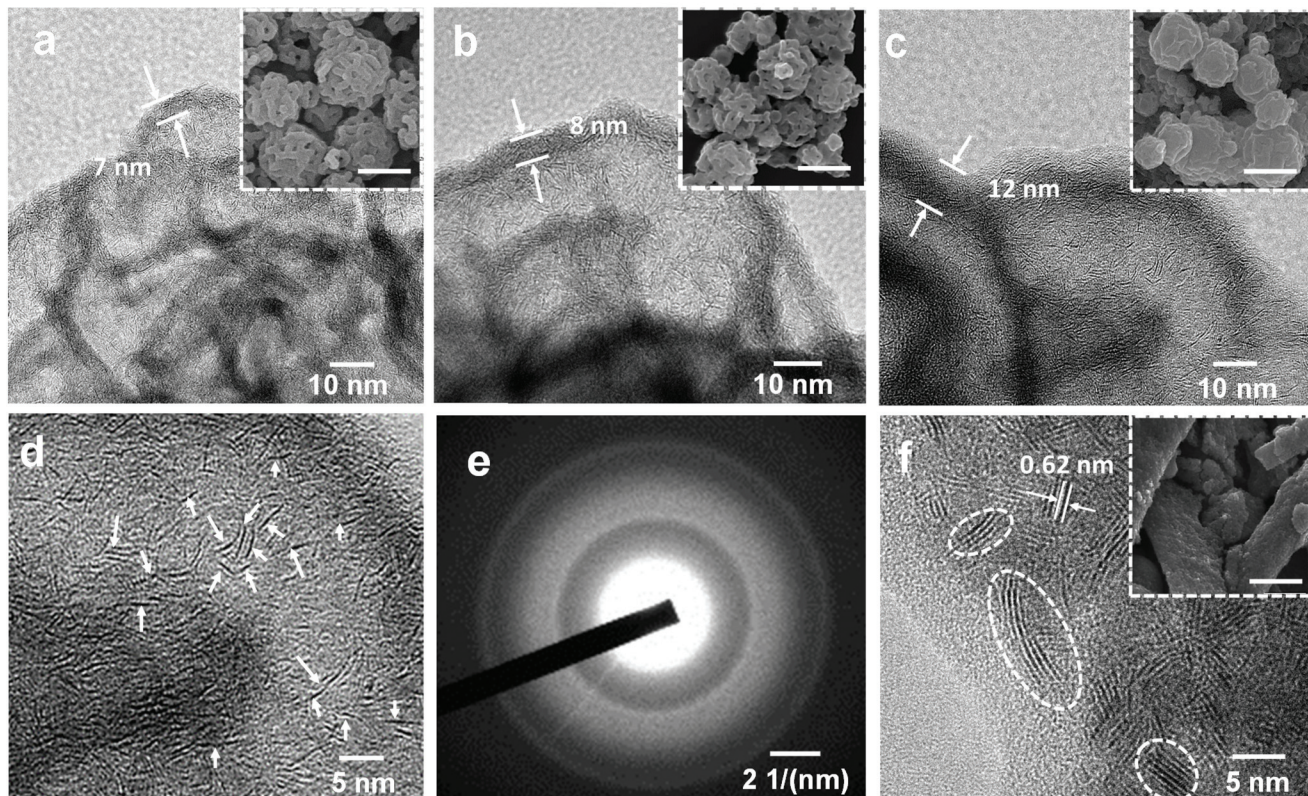


**Fig. 2** TEM images of  $\text{MoS}_2$  PNP s prepared at precursor concentrations of (a), (b) 1.5, and (c) 3  $\text{mg mL}^{-1}$ . The insets are the corresponding SEM images with a scale bar of 500 nm. (d) HRTEM image and (e) SAED pattern of  $\text{MoS}_2$ -1.5 PNP s. (f) HRTEM image of bulk  $\text{MoS}_2$  prepared without any polymer template; the inset is the corresponding SEM image with a scale bar of 500 nm.

the  $\text{MoS}_2$  nanoflakes. On the contrary, the nanoflakes of bulk  $\text{MoS}_2$  (Fig. 2f) fabricated without any polymer template show a huge tendency to fuse together, resulting in the formation of a few layers of stacked multilayers (long sheets of length  $\sim 9$  nm). Besides, an irregular bulk phase without any defined structure was found from the inset SEM image.

Taking  $\text{MoS}_2$ -1.5 PNP s, for example, the X-ray diffraction (XRD) profile verifies that  $\text{MoS}_2$  in all the PNP s exhibits a typical 2H phase (Fig. 3a, see the others in Fig. S3†).<sup>54</sup> The main diffraction peaks at  $32^\circ$  and  $56.8^\circ$  correspond to the (100) and (110) reflections, respectively. Moreover, the weak (002) reflection at  $14.4^\circ$  indicates the relatively limited layers of  $\text{MoS}_2$ . The chemical composition of the obtained  $\text{MoS}_2$ -1.5 PNP s was further confirmed by Raman spectroscopy, as shown in Fig. 3b. The two Raman peaks at  $1345$  and  $1587\text{ cm}^{-1}$  represent the D and G bands of  $\text{sp}^2$  carbon, respectively, while the Raman peaks at around  $377$  and  $403\text{ cm}^{-1}$ , correspond to the  $\text{E}_{2g}^1$  and out-of-plane  $\text{A}_g^1$  vibration modes of the  $\text{MoS}_2$ .<sup>55</sup> The amount of carbon and  $\text{MoS}_2$  was calculated based on the molybdenum oxide residue from the TGA measurement in air (Fig. 3c and S4†). The  $\text{MoS}_2$ -1.5 PNP s show  $\sim 38.9$  wt% of carbon species, corresponding to 61.1 wt% of  $\text{MoS}_2$  in the particles. In contrast,  $\sim 69.2$  wt% of  $\text{MoS}_2$  was left in the  $\text{MoS}_2$ -3 PNP s on account of higher amounts of  $\text{MoS}_4^{2-}$  precursors during coordination, as summarized in Table S1.† From the

$\text{N}_2$  adsorption/desorption isotherm curves in Fig. 3d, a distinct hysteresis loop can be observed with a typical type-IV isotherm, referring to a mesoporous structure. The pore size distribution curve displays a narrow range of mesopores centered at  $\sim 5$  nm and a broad range (10–20 nm) centered at  $\sim 15$  nm. The specific surface area ( $S_{\text{BET}}$ ) of these  $\text{MoS}_2$  particles calculated according to the BET equation is summarized in Fig. S5 and Table S2.† There is a clear decreasing tendency of  $S_{\text{BET}}$  for the  $\text{MoS}_2$ -1,  $\text{MoS}_2$ -1.5 and  $\text{MoS}_2$ -3 PNP s. The  $S_{\text{BET}}$  of  $\text{MoS}_2$ -1.5 PNP s was calculated to be  $106.6\text{ m}^2\text{ g}^{-1}$ , which is around 1.3-fold of that of the  $\text{MoS}_2$ -3 PNP s. Meanwhile, the bulk  $\text{MoS}_2$  possesses the lowest  $S_{\text{BET}}$  of  $36.3\text{ m}^2\text{ g}^{-1}$ . The  $S_{\text{BET}}$  apparently decreased with the increase in the layer thickness, mainly due to the gradually diminished gap between the thick  $\text{MoS}_2$  frameworks of the particles. Consequently, a reduced porosity as well as a lower specific surface area was obtained, as confirmed from the above-mentioned SEM and TEM images.

#### Photothermal conversion performance

To assess the photothermal conversion performance of the  $\text{MoS}_2$  particles, we monitored the temperature change of the  $\text{MoS}_2$  dispersion upon light irradiation as illustrated in Fig. 4a. A NIR-laser (808 nm,  $3\text{ W cm}^{-2}$ ) was adopted to irradiate the dispersions of the  $\text{MoS}_2$  particles placed in a quartz cuvette, while the temperature was simultaneously recorded using a



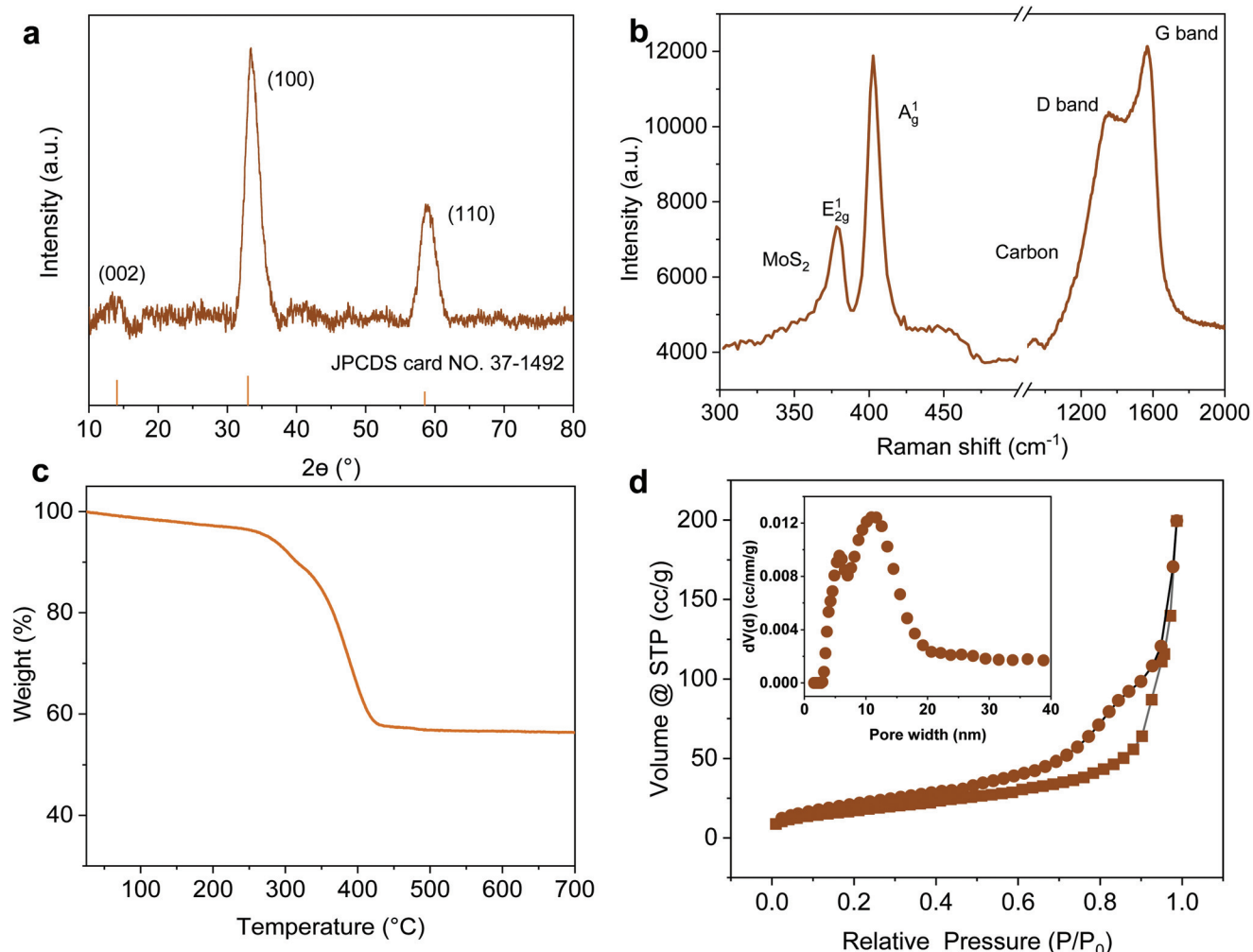
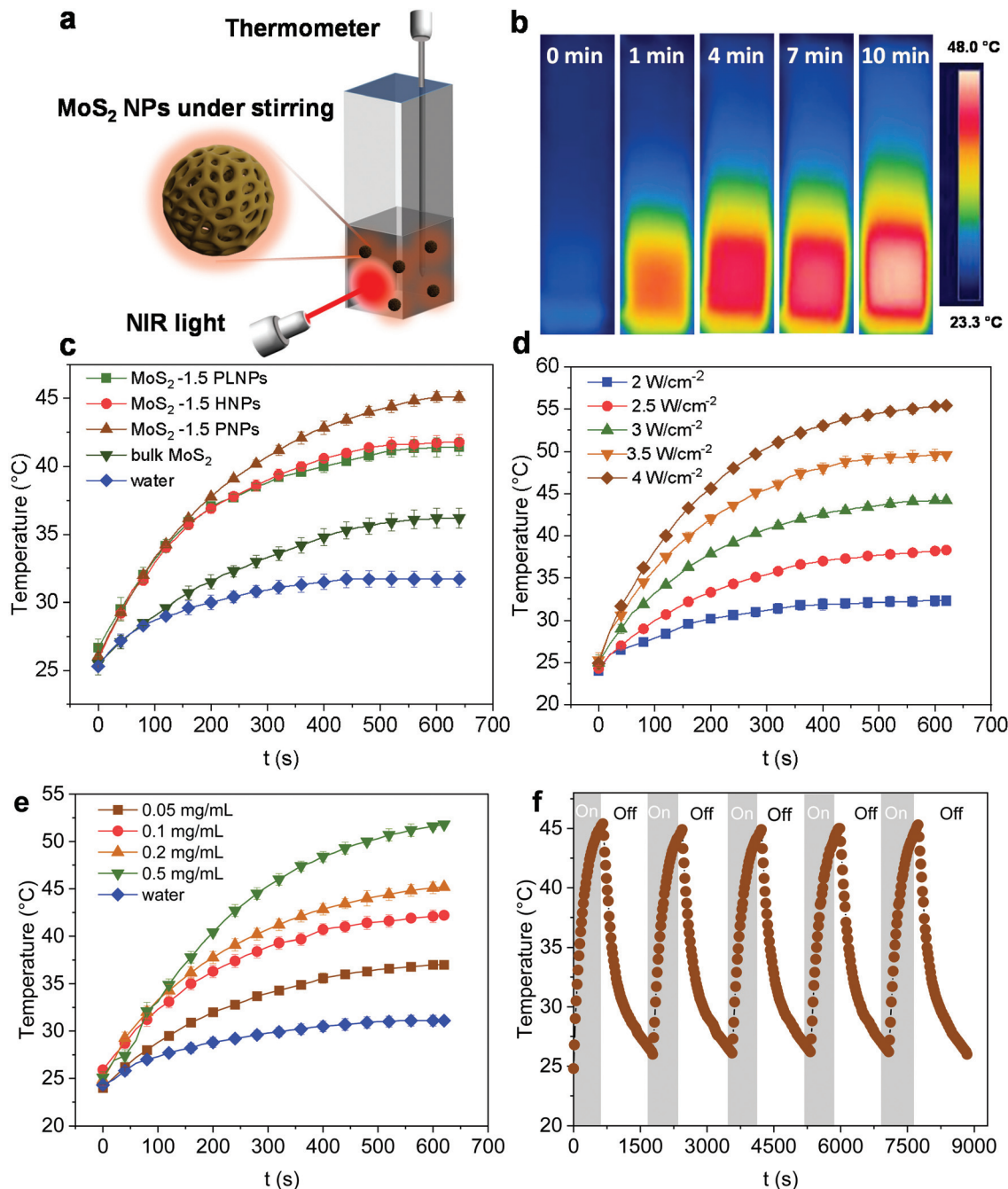


Fig. 3 (a) XRD pattern, (b) Raman spectrum, (c) TGA in air and (d) N<sub>2</sub> adsorption/desorption isotherm curves of MoS<sub>2</sub>-1.5 PNPs; the inset is the curve of pore size distribution.

thermocouple connected to a digital thermometer. The thermal evolution of the MoS<sub>2</sub>-1.5 PNP dispersion with time was first visualized using an IR camera (Fig. 4b). The temperature of MoS<sub>2</sub> particle dispersions clearly increased with the irradiation time. To precisely track the temperature variation of the MoS<sub>2</sub> dispersion during NIR irradiation, quantitative results were further collected from the digital thermometer. Fig. 4c displays the photothermal heating curves of MoS<sub>2</sub> particles fabricated with different polymer templates. The temperature of the MoS<sub>2</sub> PNP dispersion increased by ~20 °C, while the dispersion containing the same concentration of MoS<sub>2</sub>-1.5 HNPs and MoS<sub>2</sub>-1.5 PLNPs exhibited a temperature increase of ~16 °C. The bulk MoS<sub>2</sub> particle synthesized without any polymer template showed a much lower temperature increment of ~11 °C. As a reference, the pure water displayed a temperature change of ~5 °C under the same light intensity. Moreover, when the laser is off, the temperature profile of the MoS<sub>2</sub> particle dispersions decreased slowly compared to that of the bulk MoS<sub>2</sub>, showing that their defined hollow and porous structures may lead to a better thermal insulating

effect (Fig. S6†). These results indicate the dependence of the photothermal conversion performance on the surface/internal structure of the MoS<sub>2</sub> particles. It has been reported that hollow nanostructures improve the light harvesting *via* multiple scattering of the photons.<sup>56,57</sup> This, in turn, will enhance the light-to-heat conversion efficiency. The hollow architectures facilitate localization and harvesting of the light, resulting in a relatively high particle temperature. Subsequently, the solution temperature increases as the heat dissipates to the solution. Therefore, our nanostructured MoS<sub>2</sub> particles (MoS<sub>2</sub>-1.5 PLNPs, MoS<sub>2</sub>-1.5 PNPs and MoS<sub>2</sub>-1.5 HNPs) show better photothermal conversion performance than that of bulk MoS<sub>2</sub>. For MoS<sub>2</sub>-1.5 PLNPs, however, the conversion efficiency could be limited by the insufficient free space. In addition, the MoS<sub>2</sub>-1.5 PNP particles possess more complicated porous construction than that of the MoS<sub>2</sub>-1.5 HNPs, which is likely to lead to efficient light scattering and capture. The complex open architecture of the MoS<sub>2</sub>-1.5 PNPs efficiently accelerates the mass and heat transport, resulting in a higher overall temperature of the dispersion. Hence, the photothermal con-



**Fig. 4** (a) Schematic of the photothermal conversion setup. (b) Temperature variation of the  $\text{MoS}_2$ -1.5 PNP dispersion at  $0.1 \text{ mg mL}^{-1}$  visualized using an IR camera. (c) Photothermal curves of the  $\text{MoS}_2$  particles with different morphologies at  $0.1 \text{ mg mL}^{-1}$  and  $3 \text{ W cm}^{-2}$ . (d) Photothermal curves of the  $\text{MoS}_2$ -1.5 PNP dispersion at  $0.1 \text{ mg mL}^{-1}$  in response to different intensities of NIR light. (e) Photothermal curves of the  $\text{MoS}_2$ -1.5 PNP dispersion in response to different concentrations at  $3 \text{ W cm}^{-2}$ . (f) Stability test of the  $\text{MoS}_2$ -1.5 PNP dispersion at  $0.1 \text{ mg mL}^{-1}$  and  $3 \text{ W cm}^{-2}$ .

version performance of the  $\text{MoS}_2$ -1.5 PNPs stands out among these three featured  $\text{MoS}_2$  particles.

We further investigated the dependence of the photothermal effect on the irradiation power and the particle concentration. As shown in Fig. 4d, when the laser intensity increased from  $2$  to  $4 \text{ W cm}^{-2}$ , a temperature increment from  $\sim 5$  to  $\sim 32 \text{ }^{\circ}\text{C}$  was observed for the  $\text{MoS}_2$ -1.5 PNP dispersion. Additionally, when the concentration of the  $\text{MoS}_2$  PNP dis-

persion was elevated from  $0.05$  to  $0.5 \text{ mg mL}^{-1}$ , the temperature increment of the dispersions increased from  $\sim 14$  to  $\sim 29 \text{ }^{\circ}\text{C}$  under a constant laser power of  $3 \text{ W cm}^{-2}$  (Fig. 4e). This strongly implies the tunable capability of the photothermal behavior of our  $\text{MoS}_2$  particles, which is of great importance for many applications including photothermal-assisted catalysis and photothermal cancer therapy. In addition to the enhanced photothermal performance,  $\text{MoS}_2$  PNPs showed



excellent stability over a long irradiation period. The temperature increment of the particles displayed a stable reversible behavior using successive ON/OFF irradiation cycles (Fig. 4f). No obvious structural change was observed from the TEM image (Fig. S7†). It is noteworthy that the dispersions of the  $\text{MoS}_2$  PNP s with different wall thicknesses exhibited similar photothermal conversion performances and a temperature  $\sim 10$  °C higher than that of the bulk  $\text{MoS}_2$  dispersion under the same irradiation conditions (Fig. S8†).

### Catalytic reduction of 4-Nip

As a classic model reaction, the reduction of 4-Nip into 4-aminophenol (4-Amp) can be conducted under ambient conditions by  $\text{NaBH}_4$  in the presence of a catalyst. In addition, this reduction reaction can be facilely monitored by UV-vis absorption spectroscopy and commonly used as a benchmark to compare the catalytic performance of various catalysts.<sup>58,59</sup> In this work, this model reaction was employed to unfold the catalytic efficiency of our  $\text{MoS}_2$  particles with different morphologies. Importantly, we also evaluated the catalytic performance under NIR irradiation by taking advantage of the high photothermal efficiency of the  $\text{MoS}_2$  particles. Unlike conventional heating over a large macroscopic area, nanoscale heating by laser irradiation highly localizes the heat around the particles compared to the bulk solution and, therefore, might accelerate the rate of surface catalytic reactions.<sup>60,61</sup> It is noteworthy that the distinctive structure of the porous surface as well as the interconnected hollow channels in the  $\text{MoS}_2$  PNP s increases the exposed active  $\text{MoS}_2$  edges and accessible surface area for the catalytic surface reactions. In addition, these open porous particles also exhibit excellent photothermal performance. On the basis of these considerations, the catalytic performance of  $\text{MoS}_2$  PNP s was thereafter explored in the presence/absence of NIR light.

Fig. 5a displays the typical time-dependent UV-vis absorption spectra of 4-Nip after introducing  $\text{MoS}_2$  PNP s particles as catalysts. As shown, at time zero, a distinct peak of the absorption spectrum is located at 400 nm, assigned to the 4-nitrophenolate ions.<sup>62</sup> As the reaction proceeds, a new peak appears at 290 nm and increases in absorption intensity, confirming the gradual reduction of 4-Nip into 4-Amp. After 15 minutes, the absorption peak of the 4-Nip at 400 nm was diminished, revealing that 4-Nip molecules were completely converted into 4-Amp. First, the reaction was performed in the darkness to compare the catalytic activity of the three  $\text{MoS}_2$  PNP s with different wall thicknesses by comparing the reaction rates, as shown in Fig. 5b. The pseudo-first-order reaction was ensured by an excess amount of  $\text{NaBH}_4$  and the apparent reduction rate ( $k_{\text{app}}$ ) of 4-Nip was calculated by monitoring the absorbance intensity at 400 nm over time according to eqn (1):<sup>28</sup>

$$\ln \frac{c}{c_0} = \ln \frac{I}{I_0} = -k_{\text{app}} t \quad (1)$$

where  $c$  and  $c_0$  are the concentrations and  $I$  and  $I_0$  are the absorption intensities at 400 nm of 4-Nip at time  $t$  and the start of the reaction, respectively.  $k_{\text{app}}$  is the apparent rate con-

stant, which is directly obtained from the linear relationship between  $\ln(c/c_0)$  and  $t$ . Fig. 5b shows a comparison of the reaction rate constants using different  $\text{MoS}_2$  particles as a function of the catalyst concentration (see summary of  $k_{\text{app}}$  in Table S3†). Notably,  $\text{MoS}_2$ -1.5 PNP s displayed the highest catalytic performance among the various  $\text{MoS}_2$  PNP s. In contrast, the  $\text{MoS}_2$ -3 PNP s exhibited the lowest rate constant with different catalyst concentrations, which is very similar to that of the bulk  $\text{MoS}_2$  particles. It is worth noting that the  $\text{MoS}_2$ -1 PNP s are relatively easy to aggregate and cluster in aqueous dispersions, which could deteriorate their catalytic performance (Fig. S9†). Therefore, we speculate that small clusters could also form microscopically at a short time scale (15 min), which relatively limits the accessible active surface of  $\text{MoS}_2$  particles. No doubt that a larger surface area is more favorable for the surface-catalyzed reduction reaction, which can boost the reaction kinetics by providing more accessible catalytic sites. However, the overall reaction rate is determined by a series of factors, including but not limited to, accessible surface area, total active sites, and medium transfer pathway. Thus, the substantial catalytic enhancement of the  $\text{MoS}_2$ -1.5 PNP s is attributed to the porosity of the particles as well as to the accessibility of the reactant 4-Nip molecules to the internal active sites. The use of excess amount of  $\text{MoS}_4^{2-}$  precursor in the  $\text{MoS}_2$ -3 PNP s relatively reduced the surface porosity of the synthesis template (PS<sub>48.5k</sub>-b-P2VP<sub>16.5k</sub> swollen at 75 °C), which hinders the diffusion of 4-Nip molecules and retards their reactivity. The stability and the recyclability of the catalyst represent another important parameter required for the practical applications. In this work, the stability of  $\text{MoS}_2$ -1.5 PNP s was investigated, where the particles were recovered and reused for five consecutive catalytic cycles. As shown in Fig. 5c, the conversion efficiency of particles remained above 90% after five cycles, suggesting the excellent catalytic stability of the particles, which makes it possible for them to serve as efficient and reusable nanocatalysts. Moreover, no visible changes were observed in the morphology of  $\text{MoS}_2$ -1.5 PNP s after 5 catalytic cycles, as examined by TEM (Fig. 5d, S10a and 10b†). In addition, the XRD patterns of the particles remained unchanged after being utilized for the catalytic reaction (Fig. S10c†), demonstrating their good chemical stability. Collectively, the structural and chemical stability contribute to the catalytic stability of  $\text{MoS}_2$  during recycling.

Furthermore, the effect of the photoheating on the catalytic performance of the particles under light irradiation was explored. The  $\text{MoS}_2$ -1.5 PNP s were utilized for the catalytic measurements with light due to the best catalytic performance in the darkness at room temperature. The  $\text{MoS}_2$ -1.5 PNP dispersion was first continuously stirred and irradiated with NIR light for 15 minutes to ensure a stable temperature (here 37 °C; Fig. S11a†). The catalytic reduction of 4-Nip was then triggered after the introduction of  $\text{NaBH}_4$  under continuous light irradiation, and the reaction was simultaneously monitored using UV-vis spectroscopy (Fig. S11b†). It is worth mentioning that the absorption of 4-Nip showed no changes in the absence of  $\text{NaBH}_4$ , indicating that the light solely cannot



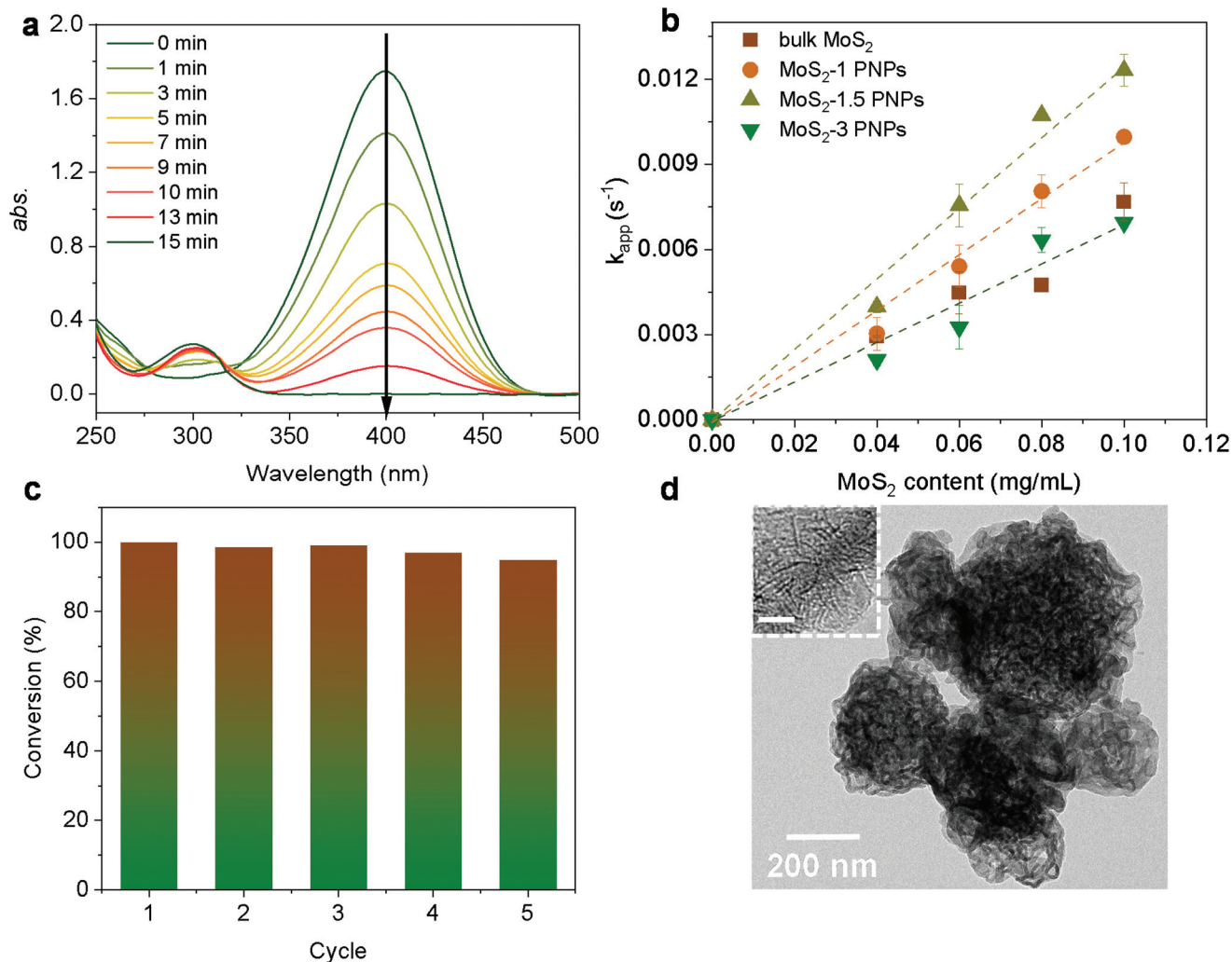


**Fig. 5** (a) UV-vis absorption spectra of the reduction of 4-Nip with the concentration of the  $\text{MoS}_2$ -1.5 PNPs at  $0.05 \text{ mg mL}^{-1}$ , 4-Nip at  $0.1 \text{ mM}$ , and  $\text{NaBH}_4$  at  $20 \text{ mM}$  at room temperature. (b) Rate constants,  $k_{app}$ , of different  $\text{MoS}_2$  PNPs as a function of catalytic concentration. (c) Catalytic recycling test of the  $\text{MoS}_2$ -1.5 PNPs at  $0.05 \text{ mg mL}^{-1}$ . (d) TEM image of the  $\text{MoS}_2$ -1.5 PNPs after the recycling tests; the inset is the corresponding HRTEM image with a scale bar of  $5 \text{ nm}$ .

initiate the reaction (Fig. S11c and 11d†). As shown in Fig. 6a and S12,† light irradiation has led to a higher reduction rate of  $0.012 \text{ s}^{-1}$ , which obviously surpassed the rate of the reaction performed in the darkness ( $0.003 \text{ s}^{-1}$ ). The temperature of the reaction solution also increased from  $20$  to  $37 \text{ }^\circ\text{C}$  by light irradiation. The enhanced reaction rate could therefore be ascribed to the high temperature induced by the photothermal conversion performance of the  $\text{MoS}_2$  particles. To elucidate the role of the photoheating effect, the reaction was performed in the darkness with external heating at  $37 \text{ }^\circ\text{C}$  in a water bath, as observed in the irradiation experiment. As a result, the reaction rate increased from  $0.003$  to  $0.008 \text{ s}^{-1}$ , suggesting the strong influence of the operating temperature. However, the reaction rate is still much lower than that of the photo-irradiated samples. It is also worth mentioning that photo-generated charges could possibly contribute to the reaction and enhance the reduction rate.<sup>63</sup> If this is true, the activation

energy ( $E_a$ ) of the reaction should be reduced significantly.<sup>64</sup> To ease this concern, we compared the  $E_a$  of the reaction in the presence/absence of light. The reactions were conducted at different operating temperatures with/without light irradiation and the corresponding reaction rates were further determined from the linear slope of  $\ln(c/c_0) \text{ vs. } t$ , as shown in Fig. 6b and c. These reaction rates were determined in the form of a typical Arrhenius plot in Fig. 6d (see summary of  $k_{app}$  in Table S4†) to calculate the  $E_a$  from the linear slopes according to the following eqn (2):<sup>65</sup>

$$-\ln(k_{app}) = \frac{E_a}{RT} - \ln(A) \quad (2)$$

where  $T$  is the total solution temperature in Kelvin,  $R$  is the gas constant,  $k_{app}$  is the apparent rate constant and  $A$  is the Arrhenius pre-factor. Thus, a significant reduction of the  $E_a$  upon illumination would be plausibly expected if the photo-



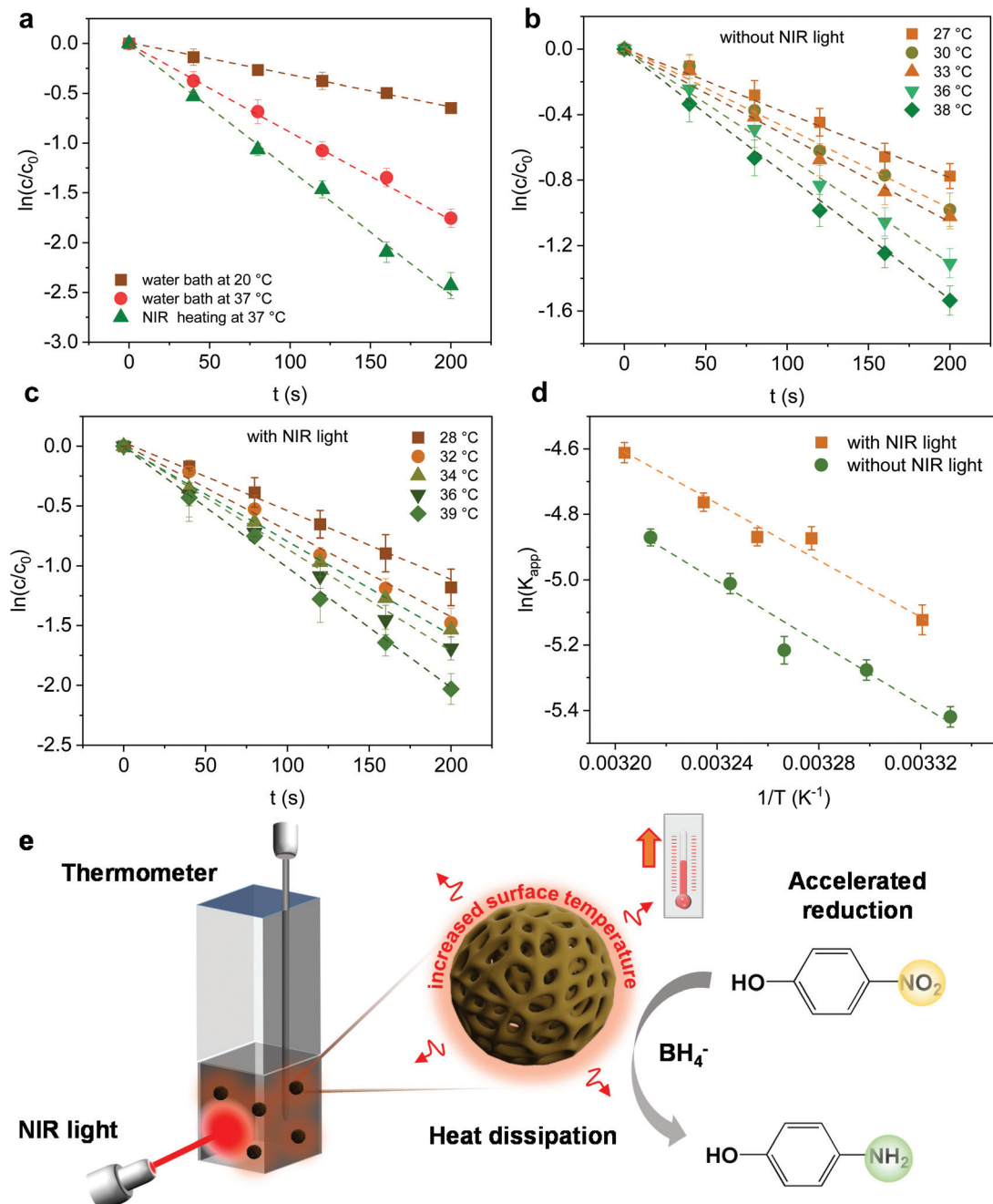
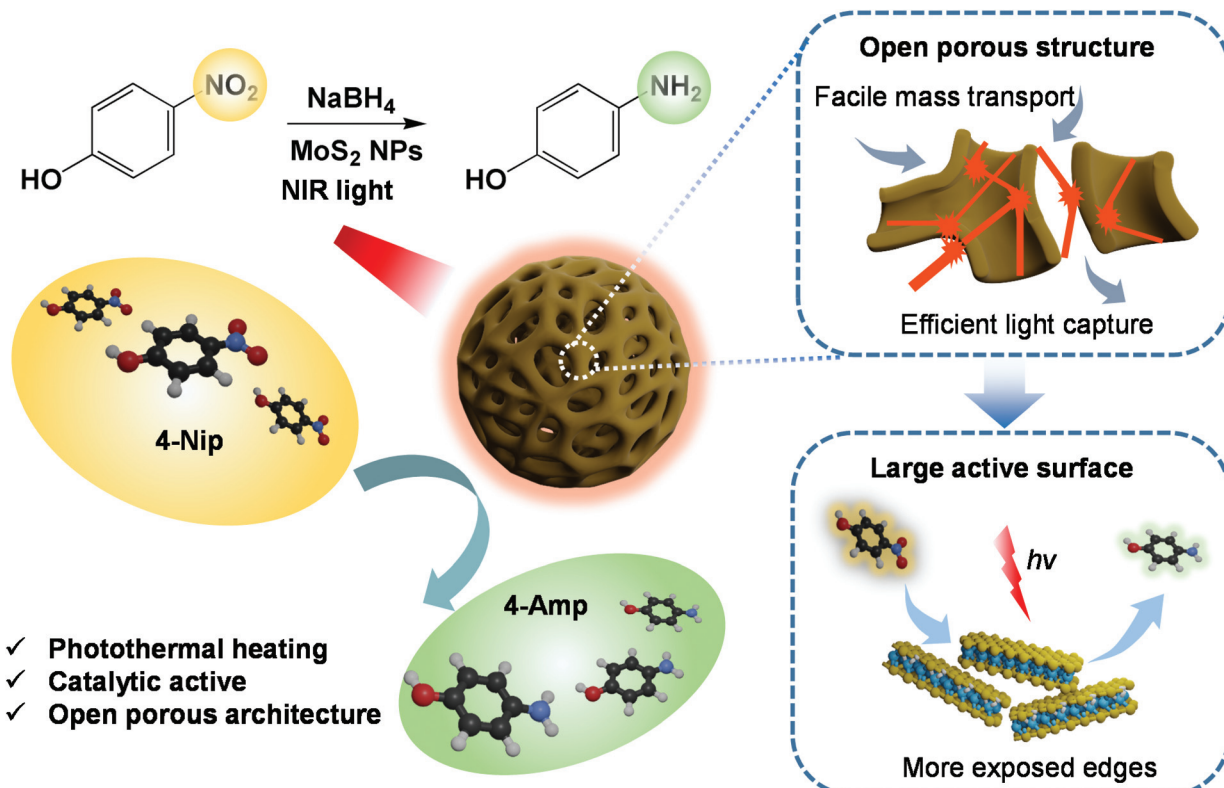


**Fig. 6** (a) Plots of  $c/c_0$  versus reaction time with the concentration of MoS<sub>2</sub>-1.5 PNPs at 0.05 mg mL<sup>-1</sup>, 4-Nip at 1 mM, and NaBH<sub>4</sub> at 0.2 M under different heating conditions. (b) Plots of  $I/I_0$  versus reaction time in the darkness. (c) Plots of  $I/I_0$  versus reaction time in the presence of light. (d) Reaction rates as a function of temperature in the presence (yellow line) and absence (green line) of 808 nm laser irradiation. The concentrations of MoS<sub>2</sub>-1.5 PNPs, 4-Nip and NaBH<sub>4</sub> are 0.03 mg mL<sup>-1</sup>, 1 mM and 0.2 M, respectively. (e) Scheme of the reduction reaction of 4-Nip under NIR irradiation.

generated charges are involved in the reaction. In the current study, however, the  $E_a$  in the presence/absence of light was calculated to be  $34.7 \pm 3.6$  and  $38.7 \pm 4.6$  kJ mol<sup>-1</sup>, respectively. The comparable results of  $E_a$  point out that the photoheating effect could be the dominant mechanism of the reaction acceleration. In conclusion, the reduction reaction of 4-Nip into 4-Amp has been reported to occur on the particle surface fol-

lowing the Langmuir–Hinshelwood model,<sup>66</sup> as NaBH<sub>4</sub> provides the reactants with the necessary hydrogen species (Fig. 6e). The borohydride ions adsorb onto the catalytic surface to produce active hydrogen species, which subsequently reduce the adsorbed 4-Nip molecules into 4-Amp. Considering that the reduction of 4-Nip is a temperature-dependent process, the reaction rate is therefore enhanced by



Scheme 2 Schematic of 4-Nip reduction with porous  $\text{MoS}_2$  under NIR light illumination.

the increased reaction temperature benefiting from the surface local heat of the  $\text{MoS}_2$  particles.<sup>67</sup> Overall, we demonstrate that our  $\text{MoS}_2$  catalysts with well-designed porous nanostructures can serve as efficient dual-functional catalysts for the enhanced reduction of 4-Nip, benefiting from the fast diffusion of reactants,<sup>68,69</sup> photo-induced heat and improved utility of active surface (Scheme 2). In other words, combining with the intrinsically catalytic property of  $\text{MoS}_2$ , the strong photoheating effect induced by NIR light irradiation further greatly accelerates the catalytic reduction reaction. The porous nanostructure of  $\text{MoS}_2$  enables the dual-functional  $\text{MoS}_2$  to be employed in the fast degradation of 4-Nip.

## Conclusions

In summary, we have designed a series of dual-functional  $\text{MoS}_2$  particles including pomegranate-like, hollow, and open porous particles using a soft  $\text{PS}-b-\text{P2VP}$  template. These nanoparticles with different well-defined internal structures show an efficient photoheating effect. The porous  $\text{MoS}_2$  nanoparticles displayed the highest photothermal conversion performance, benefitting from the localization of the light in their internal network-like structures. Moreover, this high photothermal conversion behavior has been demonstrated to accelerate the reduction reaction of 4-Nip under NIR light irradiation, confirming the synergistic properties of these

$\text{MoS}_2$  particles. Thus, the open porous  $\text{MoS}_2$  particles with interconnecting nanochannels were shown to serve as efficient nanocatalysts, while their abundant active sites, fast reactant diffusion pathway and local surface heating play a key role in enhancing the overall catalytic performance.

## Experimental section/methods

### Assembled block copolymer nanospheres

For  $\text{PS}_{48.5\text{k}}-b-\text{P2VP}_{16.5\text{k}}$ , 40 mg of the polymer powder was dissolved in 4 mL of toluene and introduced to 80 mL of deionized water with 0.12 mL of the surfactant solution (SDS, 0.5 wt%). The mixture was left to emulsify under sonication for 30 min. The solution was then evaporated using a rotary evaporator at 40 °C in a water bath, resulting in solidified polymer nanospheres dispersed in water. To completely remove toluene, the solution was left at 40 °C overnight. The dispersion was centrifuged at 9000 rpm for 2 h, and the obtained particles were redispersed in 80 mL of ethanol. The particle dispersion was further heated at 50 and 75 °C for 1 h to induce the porous structure, respectively. After cooling down, the polymer dispersion was then evaporated to remove ethanol. For  $\text{PS}_{38.5\text{k}}-b-\text{P2VP}_{23\text{k}}$ , the particles were obtained using the same protocol, while the swelling of the polymer was only performed in ethanol at 50 °C.

## Nanostructured MoS<sub>2</sub> particles

First, 150 mL of (NH<sub>4</sub>)<sub>2</sub>MoS<sub>4</sub> solution was added to the as-prepared polymer dispersion (30 mg mL<sup>-1</sup>, 15 mL) with final concentrations of (NH<sub>4</sub>)<sub>2</sub>MoS<sub>4</sub> maintained at 1, 1.5 and 3 mg mL<sup>-1</sup>, respectively. After stirring at 250 rpm for 30 min, HCl (0.16 mL, 1 M) was added dropwise into the solution, resulting in the decomposition of a slight amount of the precursor into molybdenum sulfide (MoS<sub>x</sub>,  $x = 2-3$ ). To improve the hydrophilicity of MoS<sub>2</sub> in the aqueous solution, 100  $\mu$ L of 3-MPA was added into the solution under stirring. After stirring for 30 min, the brown solution was separated by centrifugation at 8000 rpm for 40 min and washed three times with fresh water. The obtained dark brown particles were freeze-dried overnight. The final product of MoS<sub>2</sub> particles was obtained by calcination at 500 °C in an argon atmosphere for 2 h at a rate of 3 °C min<sup>-1</sup>. In comparison to MoS<sub>2</sub> particles prepared with different polymer templates, bulk MoS<sub>2</sub> was fabricated by following the same process without any polymer template.

## Photothermal conversion performance

The photothermal conversion performance of the MoS<sub>2</sub> particles was measured using an aqueous dispersion of the particles with different concentrations (0.05–0.5 mg mL<sup>-1</sup>). First, 1 mL of the dispersion was placed in a quartz cuvette under 300 rpm of stirring and directly irradiated under 808 nm NIR laser (PhotonTec Berlin, turn-key 808 nm diode laser system) with different intensities (2.0–4.0 W cm<sup>-2</sup>) for approximately 10 min. To avoid direct heating by light, the thermometer was kept far away from the laser spot, while the distance between the laser spot and the thermometer was fixed at *ca.* 6 cm. The temperature changes of the dispersion were recorded using a digital thermometer (P 300 Thermometer, Dostmann electronics) every 20 seconds. The IR camera (FLIR-E8 XT) was employed to visualize the temperature changes of the dispersion every 3 min.

## Catalytic reduction of 4-nitrophenol

**Catalytic reaction in darkness.** All the solutions and dispersion were purged with fresh N<sub>2</sub> for 30 min to remove oxygen before use. An appropriate amount of MoS<sub>2</sub> aqueous dispersion (0.1–0.25 mL, 1 mg mL<sup>-1</sup>) was sonicated for 15 min and then added into a clean quartz cuvette. The 4-Nip solution (0.25 mL, 1 mM) was introduced into the MoS<sub>2</sub> dispersion under 300 rpm of stirring. The reducing agent NaBH<sub>4</sub> (0.5 mL, 0.1 M) was then quickly injected to initialize the reduction reaction at room temperature. The total volume of the dispersion was fixed at 2.5 mL. The dispersion in the cuvette was measured using an UV-vis absorption spectrophotometer (PerkinElmer, Lambda 650 spectrometer) in the darkness. For the catalytic recycling test, the MoS<sub>2</sub> catalysts after reaction in one cycle were collected by centrifugation at 9000 rpm for 15 min. Afterwards, the MoS<sub>2</sub> particles were redispersed in fresh water with sonication for 15 min and then used for the next catalytic cycle.

**Catalytic reaction in the presence of NIR light irradiation.** a MoS<sub>2</sub> particle dispersion (0.05 mL, 1 mg mL<sup>-1</sup>) was added into

a 4-Nip solution (0.5 mL, 2 mM) in the cuvette under 300 rpm of stirring. Then, 0.45 mL of fresh water was introduced into the dispersion. After irradiation with the NIR laser at an intensity of 3 W cm<sup>-2</sup> for about 15 min, the temperature of the dispersion remained constant. A freshly prepared NaBH<sub>4</sub> solution (100  $\mu$ L, 2 M) was then quickly injected into the mixed dispersion. Following this, 0.1 mL of the reaction dispersion was taken out at regular time intervals and then quickly diluted with 1.9 mL of water. The catalysts were then filtered out using a syringe filter (pore size of 0.22  $\mu$ m), and the residual solution was tested using the UV-vis absorption spectrum. For the calculation of activation energy, the MoS<sub>2</sub> dispersion (0.03 mg mL<sup>-1</sup>) was heated by an external heating plate and NIR light (2 W cm<sup>-2</sup>), and the reaction temperature was recorded using a thermometer. In comparison to the NIR-assisted reduction, the reaction without light irradiation was conducted in a water bath heating at a corresponding temperature to that under NIR light irradiation by following the same process.

## Materials characterization

X-ray diffraction analysis (XRD, Bruker D8) measurements were conducted using a monochromatic X-ray beam with CuKa radiation at a scan rate of 0.05° min<sup>-1</sup>. N<sub>2</sub> adsorption/desorption isotherms were obtained using a Quantachrome Autosorb-1 system at 77 K. The specific surface area was calculated using the Brunauer-Emmett-Teller (BET) method based on a multipoint analysis. Transmission electron microscopy (TEM) and high-resolution TEM (HRTEM) were performed using a JEOL JEM-2100 instrument operating at an accelerating voltage of 200 kV. Scanning electron microscopy (SEM) measurement was carried out using a LEO Gemini 1530 microscope operating at 5 kV. Thermogravimetric analysis (TGA) was performed using a Mettler Toledo TGA 1 Stare thermal instrument in the temperature range of 25–900 °C at a heating rate of 10 °C min<sup>-1</sup> in air. The Raman spectra were recorded using an InVia 2R9X81 Raman spectrometer equipped with a detector of Renishaw Centrus 2MYA08 and a HeNe laser (a wavelength of 532 nm).

## Conflicts of interest

The authors declare no competing financial interests.

## Acknowledgements

The authors acknowledge Mr. J. Yang at Department of Chemistry/Functional Materials, Technische Universität Berlin for the TGA measurement. The authors also thank Mr. Z. Zhang at Department of Chemistry, Humboldt-Universität zu Berlin for the Raman measurement. Y. Lu thank the Deutsche Forschungsgemeinschaft (DFG, German Research Foundation) – Project number 410871749 for financial support.



## References

- 1 X. Liu, J. Iocozzia, Y. Wang, X. Cui, Y. Chen, S. Zhao, Z. Li and Z. Lin, *Energy Environ. Sci.*, 2017, **10**, 402–434.
- 2 N. Meng, J. Ren, Y. Liu, Y. Huang, T. Petit and B. Zhang, *Energy Environ. Sci.*, 2018, **11**, 566–571.
- 3 M. Gao, L. Zhu, C. K. Peh and G. W. Ho, *Energy Environ. Sci.*, 2019, **12**, 841–864.
- 4 M. Tan, J. Wang, W. Song, J. Fang and X. Zhang, *J. Mater. Chem. A*, 2019, **7**, 1244–1251.
- 5 T. Zhang, F. Meng, M. Gao, W. L. Ong, K.-G. Haw, T. Ding, G. W. Ho and S. Kawi, *EcoMat*, 2021, **3**, e12152.
- 6 Y. Cao, M. Derakhshani, Y. Fang, G. Huang and C. Cao, *Adv. Funct. Mater.*, 2021, **31**, 2106231.
- 7 H. Liu, H.-G. Ye, M. Gao, Q. Li, Z. Liu, A.-Q. Xie, L. Zhu, G. W. Ho and S. Chen, *Adv. Sci.*, 2021, **8**, 2101232.
- 8 K. Xu, J. Wu, C. F. Tan, G. W. Ho, A. Wei and M. Hong, *Nanoscale*, 2017, **9**, 11574–11583.
- 9 S. Hu, B.-J. Liu, J.-M. Feng, C. Zong, K.-Q. Lin, X. Wang, D.-Y. Wu and B. Ren, *J. Am. Chem. Soc.*, 2018, **140**, 13680–13686.
- 10 D. Mateo, J. Albero and H. García, *Energy Environ. Sci.*, 2017, **10**, 2392–2400.
- 11 Z. Zhang, X. Jiang, B. Liu, L. Guo, N. Lu, L. Wang, J. Huang, K. Liu and B. Dong, *Adv. Mater.*, 2018, **30**, 1705221.
- 12 L. Jiang, X. Yuan, G. Zeng, J. Liang, X. Chen, H. Yu, H. Wang, Z. Wu, J. Zhang and T. Xiong, *Appl. Catal., B*, 2018, **227**, 376–385.
- 13 Y. Yang, R. Zhao, T. Zhang, K. Zhao, P. Xiao, Y. Ma, P. M. Ajayan, G. Shi and Y. Chen, *ACS Nano*, 2018, **12**, 829–835.
- 14 H. Yuan, F. Liu, G. Xue, H. Liu, Y. Wang, Y. Zhao, X. Liu, X. Zhang, L. Zhao, Z. Liu, H. Liu and W. Zhou, *Appl. Catal., B*, 2021, **283**, 119647.
- 15 Y. Chai, H. Ma, X. Ma, X. Zhang, Y. He, Y. Wang, Q. Jiang, X. Wang, J. Ji and M. Xue, *J. Mater. Chem. A*, 2020, **8**, 10891–10897.
- 16 S. Mei, X. Xu, R. D. Priestley and Y. Lu, *Chem. Sci.*, 2020, **11**, 12269–12281.
- 17 M. Zhao, T. Chen, B. He, X. Hu, J. Huang, P. Yi, Y. Wang, Y. Chen, Z. Li and X. Liu, *J. Mater. Chem. A*, 2020, **8**, 15976–15983.
- 18 S. Mei, Z. Kochovski, R. Roa, S. Gu, X. Xu, H. Yu, J. Dzubiella, M. Ballauff and Y. Lu, *Nano-Micro Lett.*, 2019, **11**, 83.
- 19 Y.-C. Chen, A.-Y. Lu, P. Lu, X. Yang, C.-M. Jiang, M. Mariano, B. Kaehr, O. Lin, A. Taylor, I. D. Sharp, L.-J. Li, S. S. Chou and V. Tung, *Adv. Mater.*, 2017, **29**, 1703863.
- 20 J. Ke, J. Liu, H. Sun, H. Zhang, X. Duan, P. Liang, X. Li, M. O. Tade, S. Liu and S. Wang, *Appl. Catal., B*, 2017, **200**, 47–55.
- 21 D. A. Reddy, H. Park, S. Hong, D. P. Kumar and T. K. Kim, *J. Mater. Chem. A*, 2017, **5**, 6981–6991.
- 22 Z. Zhou, B. Li, C. Shen, D. Wu, H. Fan, J. Zhao, H. Li, Z. Zeng, Z. Luo, L. Ma and C. Tan, *Small*, 2020, **16**, 2004173.
- 23 M.-H. Wu, L. Li, N. Liu, D.-J. Wang, Y.-C. Xue and L. Tang, *Process Saf. Environ. Prot.*, 2018, **118**, 40–58.
- 24 X. Li, L. Kong, W. Hu, C. Zhang, A. Pich, X. Shi, X. Wang and L. Xing, *J. Adv. Res.*, 2022, **37**, 255–266.
- 25 D. Xu, Z. Li, L. Li and J. Wang, *Adv. Funct. Mater.*, 2020, **30**, 2000712.
- 26 J. Wang, Y. Li, L. Deng, N. Wei, Y. Weng, S. Dong, D. Qi, J. Qiu, X. Chen and T. Wu, *Adv. Mater.*, 2017, **29**, 1603730.
- 27 X. Yang, Y. Yang, L. Fu, M. Zou, Z. Li, A. Cao and Q. Yuan, *Adv. Funct. Mater.*, 2018, **28**, 1704505.
- 28 S. García-Dalí, J. I. Paredes, J. M. Munuera, S. Villar-Rodil, A. Adawy, A. Martínez-Alonso and J. M. D. Tascón, *ACS Appl. Mater. Interfaces*, 2019, **11**, 36991–37003.
- 29 X. Hai, W. Zhou, K. Chang, H. Pang, H. Liu, L. Shi, F. Ichihara and J. Ye, *J. Mater. Chem. A*, 2017, **5**, 8591–8598.
- 30 J. Xie, H. Zhang, S. Li, R. Wang, X. Sun, M. Zhou, J. Zhou, X. W. Lou and Y. Xie, *Adv. Mater.*, 2013, **25**, 5807–5813.
- 31 W. Bao, N. J. Borys, C. Ko, J. Suh, W. Fan, A. Thron, Y. Zhang, A. Buyanin, J. Zhang and S. Cabrini, *Nat. Commun.*, 2015, **6**, 1–7.
- 32 R. Asahi, T. Morikawa, T. Ohwaki, K. Aoki and Y. Taga, *Science*, 2001, **293**, 269–271.
- 33 M. Guo, Z. Xing, T. Zhao, Z. Li, S. Yang and W. Zhou, *Appl. Catal., B*, 2019, **257**, 117913.
- 34 X. Yu, R. Du, B. Li, Y. Zhang, H. Liu, J. Qu and X. An, *Appl. Catal., B*, 2016, **182**, 504–512.
- 35 T. Quan, N. Goubard-Bretesché, E. Härk, Z. Kochovski, S. Mei, N. Pinna, M. Ballauff and Y. Lu, *Chem. – Eur. J.*, 2019, **25**, 4757–4766.
- 36 M. Xiao, Z. Wang, M. Lyu, B. Luo, S. Wang, G. Liu, H.-M. Cheng and L. Wang, *Adv. Mater.*, 2019, **31**, 1801369.
- 37 R. R. Poolakkandy and M. M. Menamparambath, *Nanoscale Adv.*, 2020, **2**, 5015–5045.
- 38 Y. Cui, T. Zhu, A. Li, B. Liu, Z. Cui, Y. Qiao, Y. Tian and D. Qiu, *ACS Appl. Mater. Interfaces*, 2018, **10**, 6956–6964.
- 39 S. Mei, L. Wang, X. Feng and Z. Jin, *Langmuir*, 2013, **29**, 4640–4646.
- 40 S. Mei and Z. Jin, *Small*, 2013, **9**, 322–329.
- 41 H. Fan and Z. Jin, *Macromolecules*, 2014, **47**, 2674–2681.
- 42 W. Han, P. Hou, S. Sadaf, H. Schäfer, L. Walder and M. Steinhart, *ACS Appl. Mater. Interfaces*, 2018, **10**, 7451–7458.
- 43 L. Guo, Y. Wang and M. Steinhart, *Chem. Soc. Rev.*, 2021, **50**, 6333–6348.
- 44 N. Hampu, J. R. Werber, W. Y. Chan, E. C. Feinberg and M. A. Hillmyer, *ACS Nano*, 2020, **14**, 16446–16471.
- 45 H. Yang, X. Shi, S. Chu, Z. Shao and Y. Wang, *Adv. Sci.*, 2021, **8**, 2003096.
- 46 D. Liu, Y. Liao, E. J. Cornel, M. Lv, T. Wu, X. Zhang, L. Fan, M. Sun, Y. Zhu, Z. Fan and J. Du, *Chem. Mater.*, 2021, **33**, 7972–7985.
- 47 E. Kang, B. Graczykowski, U. Jonas, D. Christie, L. A. G. Gray, D. Cangialosi, R. D. Priestley and G. Fytas, *Macromolecules*, 2019, **52**, 5399–5406.
- 48 Y. Wang, U. Gösele and M. Steinhart, *Chem. Mater.*, 2008, **20**, 379–381.



49 J. Zhou and Y. Wang, *Macromolecules*, 2020, **53**, 5–17.

50 Y. Liu, J. Wang, M. Zhang, H. Li and Z. Lin, *ACS Nano*, 2020, **14**, 12491–12521.

51 X. Li, J. Iocozzia, Y. Chen, S. Zhao, X. Cui, W. Wang, H. Yu, S. Lin and Z. Lin, *Angew. Chem., Int. Ed.*, 2018, **57**, 2046–2070.

52 S. Mei, J. Cao and Y. Lu, *J. Mater. Chem. A*, 2015, **3**, 3382–3389.

53 T. Quan, Y. Xu, M. Tovar, N. Goubard-Bretesché, Z. Li, Z. Kochovski, H. Kirmse, K. Skrodeczky, S. Mei, H. Yu, D. Abou-Ras, M. Wagemaker and Y. Lu, *Batter. Supercaps*, 2020, **3**, 747–756.

54 D. Yang and R. F. Frindt, *J. Appl. Phys.*, 1996, **79**, 2376–2385.

55 X. Zheng, J. Xu, K. Yan, H. Wang, Z. Wang and S. Yang, *Chem. Mater.*, 2014, **26**, 2344–2353.

56 S. H. Hwang, J. Yun and J. Jang, *Adv. Funct. Mater.*, 2014, **24**, 7619–7626.

57 J. Sun, J. Zhang, M. Zhang, M. Antonietti, X. Fu and X. Wang, *Nat. Commun.*, 2012, **3**, 1139.

58 S. Wunder, Y. Lu, M. Albrecht and M. Ballauff, *ACS Catal.*, 2011, **1**, 908–916.

59 P. Hervés, M. Pérez-Lorenzo, L. M. Liz-Marzán, J. Dzubiella, Y. Lu and M. Ballauff, *Chem. Soc. Rev.*, 2012, **41**, 5577–5587.

60 W. Feng, L. Chen, M. Qin, X. Zhou, Q. Zhang, Y. Miao, K. Qiu, Y. Zhang and C. He, *Sci. Rep.*, 2015, **5**, 17422.

61 N. R. S. Sibuyi, K. L. Moabelo, M. Meyer, M. O. Onani, A. Dube and A. M. Madiehe, *J. Nanobiotechnol.*, 2019, **17**, 122.

62 R. D. Neal, R. A. Hughes, P. Sapkota, S. Ptasinska and S. Neretina, *ACS Catal.*, 2020, **10**, 10040–10050.

63 Q. Xiao, S. Sarina, A. Bo, J. Jia, H. Liu, D. P. Arnold, Y. Huang, H. Wu and H. Zhu, *ACS Catal.*, 2014, **4**, 1725–1734.

64 N. Li, Z. Liu, M. Liu, C. Xue, Q. Chang, H. Wang, Y. Li, Z. Song and S. Hu, *Inorg. Chem.*, 2019, **58**, 5746–5752.

65 Z. A. Piskulich, O. O. Mesele and W. H. Thompson, *J. Phys. Chem. A*, 2019, **123**, 7185–7194.

66 S. Wunder, F. Polzer, Y. Lu, Y. Mei and M. Ballauff, *J. Phys. Chem. C*, 2010, **114**, 8814–8820.

67 J. Lü, Y. Fu, Y. Song, D. Wang and C. Lü, *RSC Adv.*, 2016, **6**, 14247–14252.

68 L. Forni, *Catal. Today*, 1999, **52**, 147–152.

69 Y. Zhou, Q. Ji, H. Liu and J. Qu, *Environ. Sci. Technol.*, 2018, **52**, 7477–7485.

